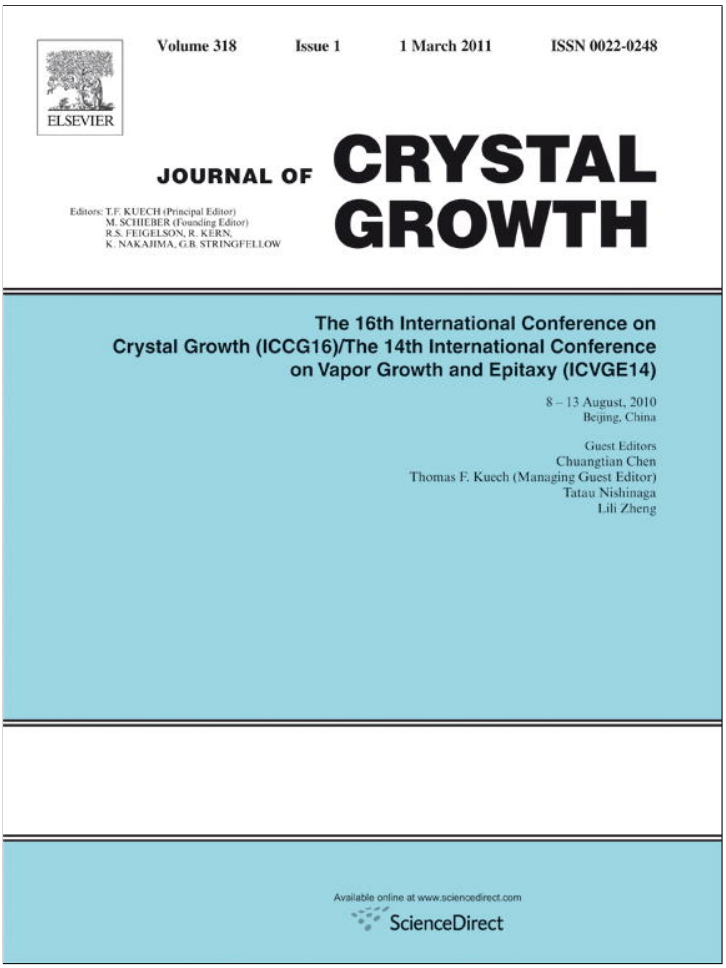

Journal of Crystal Growth 318 (2011) 674–678

Contents lists available at ScienceDirect

Journal of Crystal Growth

journal homepage: www.elsevier.com/locate/jcrysgro

Simulation and experiment on laser-heated pedestal growth of chromium-doped yttrium aluminum garnet single-crystal fiber

Chun-Lin Chang [a], Sheng-Lung Huang [a,b], Chia-Yao Lo [c], Kuang-Yao Huang [a], Chung-Wen Lan [d], Wood-Hi Cheng [e], Peng-Yi Chen [f,*]

[a] Institute of Photonics and Optoelectronics, National Taiwan University, Taipei 10617, Taiwan
[b] Department of Electrical Engineering, National Taiwan University, Taipei 10617, Taiwan
[c] Institute of Optoelectronic Sciences, National Taiwan Ocean University, Keelung 20224, Taiwan
[d] Department of Chemical Engineering, National Taiwan University, Taipei 10617, Taiwan
[e] Department of Photonics, National Sun Yat-sen University, Kaohsiung 80424, Taiwan
[f] Department of Gemology, Meiho University, Pingtung 91202, Taiwan

ARTICLE INFO

Available online 8 December 2010

Keywords:
A1. Heat transfer
A1. Fluid flows
A2. Laser heated pedestal growth
A2. Single crystal growth
B2. Yttrium compounds

ABSTRACT

The laser-heated pedestal growth (LHPG) of chromium-doped yttrium aluminum garnet (Cr:YAG) single-crystal fibers in ⟨1 1 1⟩ direction was investigated via a two-dimensional (2D) simulation which is verified by experimental observations on the interface shapes. Radial dopant profiles at the growth front in simulations were consistent with that of the grown crystal fibers in *ex-situ* measurements. The concentration level and distribution compared to the corresponding fluid flow and heat transfer were reported to visualize the phenomena that cannot be observed easily. It is viable to adjust the shape of air/melt interface, the distribution of mass flow rate, and especially the shape of growth front for acquiring a desirable radial dopant profile.

1. Introduction

Single-crystal fibers have become the subject of intense study recently [1]. They are recognized for their remarkable characteristics, such as low defect density, long mode confinement length, and good laser efficiency. These advantages enable their applications in passive devices [2,3], active devices [4–11], and nonlinear fiber devices [12–14]. For various kinds of high quality crystal fiber devices, the concentration level and distribution of dopants in the melt, especially at the growth front, are necessary to be designed and optimized finely. Therefore, the manipulation of parametric space and the system diagnostics are getting critical for growing a crystal fiber, comprehensive information is necessary to be acquired quantitatively both in experiments and simulations, especially on some intermediate behaviors near the zone boundaries.

For growing single-crystal fiber using LHPG method, there were only several simplified numerical models [15–17]. Here a 2D simulation, modified from previous model for growing bulk crystals using floating-zone method [18], has been achieved and verified by observations on the melt shapes and volume in steady state [19]. Because a non-orthogonal body-fitting grid system with the control-volume finite-difference method was employed [15], the intermediate boundary behaviors can be determined both efficiently and accurately. Moreover, heat transfer and fluid flow in the melt, which cannot be easily diagnosed precisely, were also analyzed [20].

In this paper, we report chromium (Cr) ions in yttrium aluminum garnet ($Y_3Al_5O_{12}$; YAG) crystal in a LHPG system, both experimentally and numerically, after verifying the melt shape [19] and further analysis of heat transfer and fluid flow [20]. The radial profiles of dopants at the growth front are verified by *ex-situ* measurements in similar conditions. Moreover, the influences of the reduction ratios, diffusion and surface-tension–temperature coefficient on the dopant distribution with the corresponding fluid flow and temperature distribution are discussed.

2. Experimental approach

For the setup in Fig. 1 [19,21], a 10.6-μm and $M^2 \sim 1.1$ CO_2 laser system with an attenuator to adjust laser power was the heat source to enter the growth chamber. Power fluctuation can be improved from $\pm 5\%$ to $< \pm 1\%$ using a feedback control. Inside the chamber, the incident Gaussian beam was transformed into a ring-shaped semi-Gaussian beam by a reflaxicon, which consists of an inner cone surrounded by a coaxial outer cone. The inner cone was mounted on the center of a zinc selenide (ZnSe) window. The ring-shaped beam was reflected by a planar mirror, and then tightly focused by a parabolic

* Corresponding author. Tel.: +886 8 7799821x6506.
E-mail address: x00008415@meiho.edu.tw (P.-Y. Chen).

0022-0248/$ - see front matter © 2010 Elsevier B.V. All rights reserved.
doi:10.1016/j.jcrysgro.2010.11.035

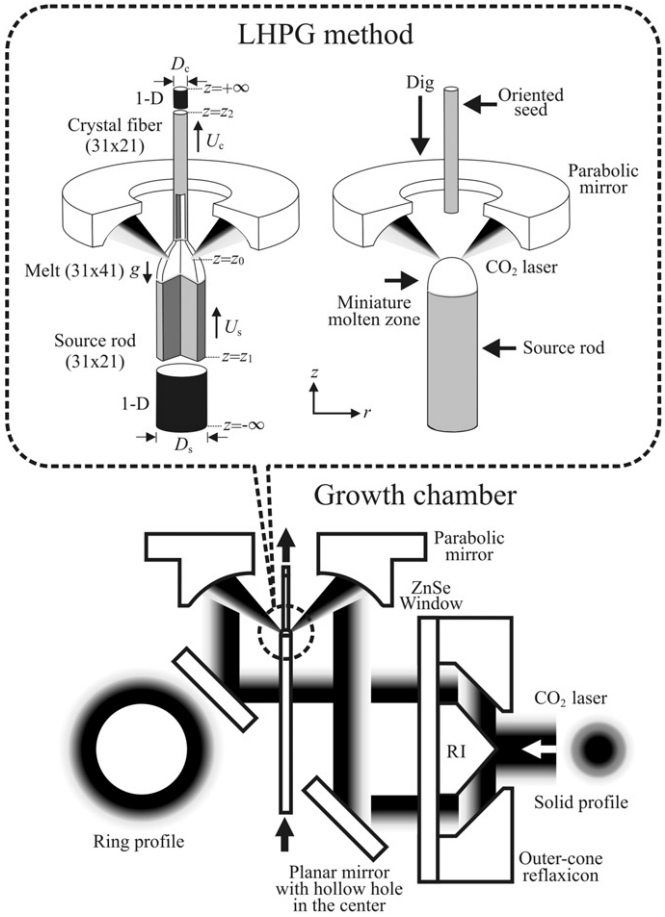

Fig. 1. Schematic illustration of LHPG method (upper) and the configuration of growth chamber (lower) for growing single-crystal fibers. RI is the inner-cone reflaxicon. z is the axial axis along the growth direction, r is the radial axis, z_1 and z_2 are the criteria of axial position sufficiently distant from the melt, $z=0$ is the axial position of laser projection, g is gravitational acceleration, and $U_{s,c}$ and $D_{s,c}$ are defined in Table 1.

mirror to melt the source rod as the pedestal. The diameter of the source rod is 300 μm with U_s=1.2 mm. The seed rod in ⟨1 1 1⟩ direction was further dipped into it to form a highly-heat-concentrated miniature melt bridge. During growth, different diameter reduction ratios were obtained by controlling the fiber-drawing speed according to mass conservation. The source rods used here were cut from YAG crystals, contained a mixture of ~0.25 wt% chromium (III) oxide (Cr_2O_3) and < 0.1 wt% calcium(II) oxide (CaO) [22].

3. Mathematical formulation

The physical properties of YAG material and other related input parameters are shown in Table 1 [23]. Four governing equations are listed as follows:

Equation of motion:

$$\frac{\partial}{\partial r}\left(\frac{\omega}{r}\frac{\partial\psi}{\partial z}\right)-\frac{\partial}{\partial z}\left(\frac{\omega}{r}\frac{\partial\psi}{\partial r}\right)+\frac{\partial}{\partial r}\left[\frac{1}{r}\frac{\partial}{\partial r}(\mu_{\mathrm{m}}r\omega)\right]+\frac{\partial}{\partial z}\left[\frac{1}{r}\frac{\partial}{\partial r}(\mu_{\mathrm{m}}r\omega)\right]-\rho_{\mathrm{m}}\beta_{\mathrm{m}}g\frac{\partial T}{\partial r}=0. \quad (1)$$

Stream equation:

$$\frac{\partial}{\partial z}\left(\frac{1}{\rho_{\mathrm{m}}r}\frac{\partial\psi}{\partial z}\right)+\frac{\partial}{\partial r}\left(\frac{1}{\rho_{\mathrm{m}}r}\frac{\partial\psi}{\partial r}\right)+\omega=0. \quad (2)$$

Table 1
YAG physical properties and other related input parameters.

Items	Value	Symbol & Unit
Density of the solid	3.685	ρ_s (g cm^{-3})
Density of the melt	4.3	ρ_m (g cm^{-3})
Melting point	2243.2	T_m (K)
Melt/solid latent heat	455.5	ΔH (J g^{-1})
Thermal conductivity of the solid	0.1[a]	k_s (W cm^{-1} K^{-1})
Thermal conductivity of the melt	0.1[a]	k_m (W cm^{-1} K^{-1})
Specific heat of solid	1.0[a]	C_{ps} (J g^{-1} K^{-1})
Specific heat of melt	0.39[a]	C_{pm} (J g^{-1} K^{-1})
Surface tension	780[a]	Γ (dyn cm^{-1})
Surface-tension–temperature coefficient	−0.035[a]	$\partial\gamma/\partial T$ (dyn cm^{-1} K^{-1})
Viscosity of the melt	0.4	μ_m (g cm^{-1} s^{-1})
Thermal expansion coefficient of the melt	6.5×10^{-5}	β_m (K^{-1})
Radiation emissivity of the solid	0.7	ε_s
Radiation emissivity of the melt	0.5	ε_m
Segregation coefficient	3.2	K
Diffusion coefficient	10^{-2}	D (cm^2 s^{-1})
Other input parameters		
Diameter of rod and fiber	300/300,105,75[b]	D_s/D_c (μm)
Speeds of feed and growth	1.2/1.2, 9.6, 19.2[b]	U_s/U_c (μm s^{-1})
Rod length	5	L (cm)
Heat transfer coefficient	1.1×10^{-3}	h (W cm^{-2} K^{-1})
Ambient constant temperature	575-650	T_a(K)

[a] At melting point.
[b] Corresponding to reduction ratio of 100, 35, 25%.

Energy equation:

$$\frac{\partial}{\partial r}\left(C_{\mathrm{pm}}T\frac{\partial\psi}{\partial z}\right)-\frac{\partial}{\partial z}\left(C_{\mathrm{pm}}T\frac{\partial\psi}{\partial r}\right)+\frac{\partial}{\partial z}\left(rk_{s,m}\frac{\partial T}{\partial z}\right)+\frac{\partial}{\partial r}\left(rk_{s,m}\frac{\partial T}{\partial r}\right)=0. \quad (3)$$

Mass-balance equation [24]:

$$\frac{\partial}{\partial r}\left(\frac{C_m}{\rho_m}\frac{\partial\psi}{\partial z}\right)-\frac{\partial}{\partial z}\left(\frac{C_m}{\rho_m}\frac{\partial\psi}{\partial r}\right)+\frac{\partial}{\partial z}\left(rD\frac{\partial C_m}{\partial z}\right)+\frac{\partial}{\partial r}\left(rD\frac{\partial C_m}{\partial r}\right)=0. \quad (4)$$

where ω is the vorticity, ψ is the stream function, T is the temperature, C_{m} is the dopant concentration of the melt and D is the diffusion coefficient of dopants in the melt. Three boundary conditions of thermal flux and fluid flow [19] are involved for (1) along z axis, (2) at the growth and feed front, and (3) on the surfaces of the source rod, melt, and crystal fiber. The feed front is noted as the lower melt/solid interface near the source rod and the growth front is noted as the upper one near the crystal fiber. Moreover, there is additional thermal condition for the position far away from the melt [20]. The experimental verification of melt volume and shape indicates radiative transport in the melt is not significant because of the miniature volume and high absorption at 10.6-μm. Here, only modified boundary conditions for considering the dopants are presented as follows [24]:

(1) Along the z axis

$$\partial C/\partial r=0, \quad (5)$$

(2) At the growth front

$$D(\vec{n}_g\cdot\nabla C_m)=U_c(C_m-KC_m)\vec{n}_g\cdot\vec{e}_z \quad \text{with} \quad T=T_m+mC_m, \quad (6)$$

(3) At the feed front

$$D(\vec{n}_f\cdot\nabla C_m)=U_s(C_m-C_s)\vec{n}_f\cdot\vec{e}_z \quad \text{with} \quad T=T_m+mC_m, \quad (7)$$

where $\vec{n}_{f,g}$ and $C_{s,c}$ are a unit normal vectors toward the melt and the dopant concentration of the source rod or the crystal fiber, respectively, at the feed or growth front $K=C_c/C_m$ is the segregation coefficient according to the phase diagram, $\vec{e}_z$ is the unit vector along z axis, and m is the slope of liquids line in the phase diagram. In Eqs. (6) and (7), diffusion in the crystal is neglected.

(4) At the air/melt interface of melt zone

$$\vec{n}_m \cdot \nabla C = 0, \tag{8}$$

where $\vec{n}_m$ is a unit normal vector at the air/melt surface. The surface tension–concentration coefficient is set to zero. The influence on the melt shapes is absent whether mass-balance equation is considered or not. At the steady-state melt/solid interfaces, the average dopant concentration of crystal fiber is the same as that of source rod, and is K times higher than that of the melt.

A 2D curvilinear coordinate system transformed from the cylindrical one is adopted for efficient calculations on the curved interfaces. Except for the transformation of ψ, ω and T [19], we add the transformation of concentration C with the algebraic coefficients $a=1/\rho_m$, $b=rD$, $c=1$, and $d=0$. Owing to the non-uniform grid spaces in physical domain, finer fitting near the interfaces makes the fluid flow and temperature distribution more accurate. The governing equations and their boundary conditions after coordinate transformation can be solved in computational domain using the control-volume finite difference method. In order to reduce the computational load without compromising on accuracy, the system is divided into three regions as shown in Fig. 1, namely an outer region in crystal fiber ($z_2 < z \le +\infty$) and source rod ($-\infty \le z < z_1$), and an inner region comprising melt and nearby solid ($z_1 \le z \le z_2$). The temperature distribution is essentially 2D in the inner region, while the heat transfer is 1D in the two outer regions. Along the crystal fiber and source rod, the temperature distribution, dominated by heat conduction, decays exponentially from the melt, and the decay rate is function of fiber diameter [20]. In addition, the consistency of melt/solid interface shape between experiments and simulations [19] also indicates that the radiative transfer in the solid phase can be neglected when the Biot number ($=h \cdot D_{s,c}/k_s$) is $\sim 10^{-6}$ [17]. Here the reduction ratio ($R_\%$) is defined as D_c/D_s and the speed ratio is defined as U_c/U_s. More details can be found in our previous works [19,20].

4. Results and discussion

Fig. 2(a) shows a comparison between the Cr^{3+} fluorescent intensity profile, measured by laser scanning confocal microscopy (LSCM) [25] and the concentration of chromium (III) oxide (Cr_2O_3), measured using an electron probe micro-analyzer (EPMA) for calibration. LSCM permits measurement of the characteristic spectrum of Cr^{3+} ion using a confocal microscope with a 532-nm frequency-doubled Nd:YVO_4 laser acting as light source for pumping the Cr^{3+} ions to scan the fluorescent intensity profile across the fiber cross section. The LSCM sensitivity was calibrated as 4.4×10^{-4} wt% with 0.1-s/pixel measurement time. The measurements of total Cr_2O_3 concentration, using EPMA, which cannot distinguish between the oxidation states, are also achieved with the sensitivity of 0.01 wt% and a 240-s/spot measurement time. Comparing Cr^{3+} and Cr^{4+} fluorescence shows most of the Cr ions are Cr^{3+}. The radial dopant profiles are able to reflect that of Cr_2O_3. Fig. 2 (b) shows the radial dopant profiles at growth front in simulations are consistent with that of grown crystal fibers in *ex-situ* measurements. As the allowable power (P_{allow}) decreases, the radial profile becomes smooth and even convex outward. It is noted

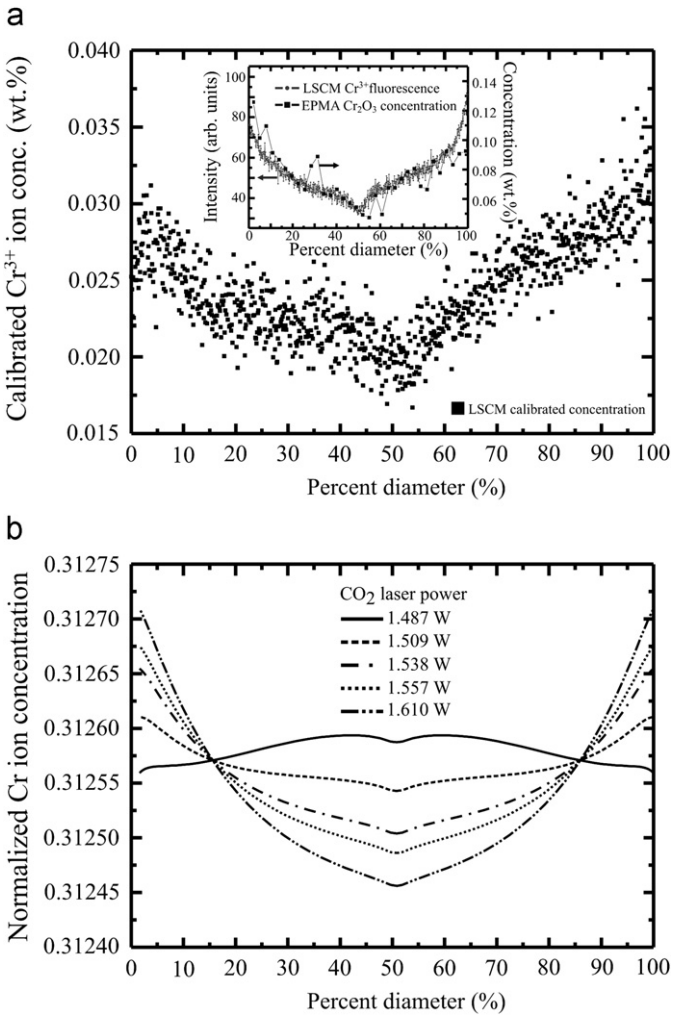

Fig. 2. In percent diameter plot, (a) In experiments, the calibrated concentration of Cr^{3+} ions across the fiber cross sections for $D_s=66$ μm and $R_\%=22\%$ measured by LSCM. The inset shows comparison and calibration between Cr^{3+} fluorescent intensity profile measured by LSCM and the concentration of Cr_2O_3 measured by EPMA. (b) In simulations, the normalized radial dopant profiles of Cr ions at the growth front at various P_{allow} for $R_\%=35\%$ while $K=3.2$ [26], $D=10^{-2}$ cm^2 s^{-1}, and $\partial\gamma/\partial T=-3.5\times10^{-2}$ dyn cm^{-1} K^{-1} [27].

that the shapes of growth front and air/melt interface, dominant by P_{allow} and $R_\%$, rather than fluid flow determine the radial dopant profile.

In Fig. 3, the Cr ions are getting denser from the growth to feed front due to segregation effect and accumulate more near the feed front when $R_\%$ decreases. The intervals of concentration contour lines are uniform and symmetric for $R_\%=100\%$. On decreasing $R_\%$, the interval gets narrower near the growth front and wider near the feed front. It is noted that the interval is proportional to the dopant diffusion velocity, depending on $R_\%$, due to the continuity. The contour inclination occurs owing to the deformation of air/melt interface when $R_\%$ or P_{allow} decreases. The contour lines are always perpendicular to both air/melt interface and z axis defined by Eqs. (5) and (8) if the 2D model is without perturbation and vaporization at the air/melt interface, respectively. For the miniature melt zone with much smaller air/melt surface area, this assumption is closer to the real conditions compared to the bulk crystal growth [24]. The corresponding normalized radial concentration profiles of Cr ions at the growth front are for $R_\%=100\%$, 35%, and 25% in Fig. 3 (g)-(i) at high and low P_{allow}. Both the inclination of contour lines and the profile of growth front determine the radial dopant profiles. From low to high P_{allow}, the growth front and air/melt interface become

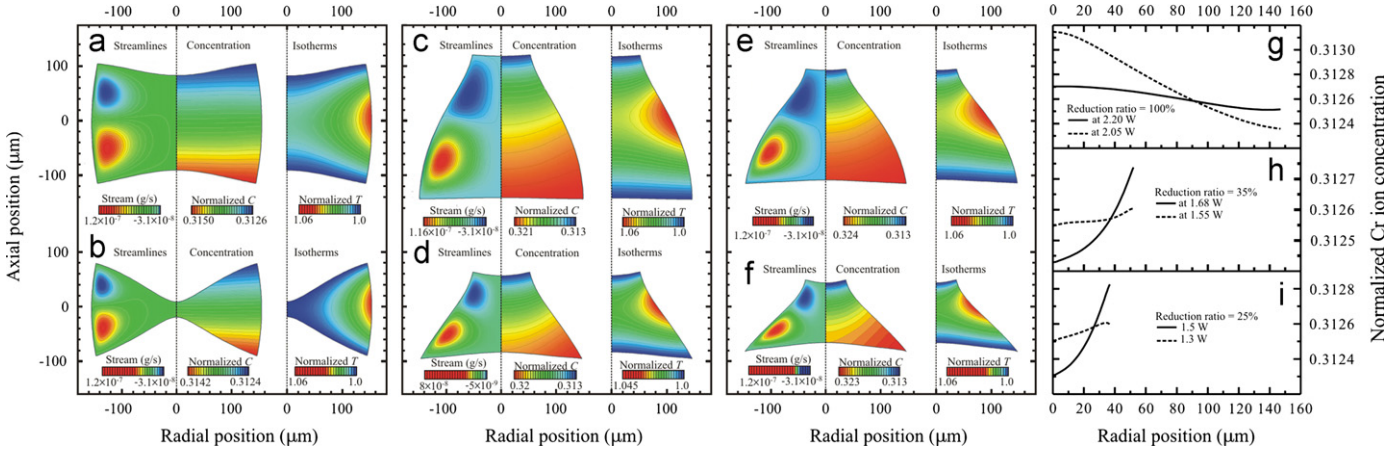

Fig. 3. The streamlines (left), normalized radial concentration of Cr ions (middle), and isotherms (right) in the miniature melt zones at high (top row) and low (bottom row) P_{allow} for $R_{\%}$=(a)(b) 100%, (c)(d) 35%, and (e)(f) 25% while K=3.2, $\partial\gamma/\partial T = -3.5\times10^{-2}$ dyn cm^{-1} K^{-1} and $D=10^{-2}$ cm^2 s^{-1}.The corresponding normalized radial profiles at the growth front are for $R_{\%}$= (g) 100%, (h) 35%, and (i) 25%. The solid and dash lines are at high and low P_{allow}, respectively. The left color bars of the fluid flow in the unit of g s^{-1} are positive for counterclockwise loop or $z>0$ direction and vice versa. The middle ones present the dopant concentration with the initial normalized value of unity before melting. The right ones used for the temperature distribution are normalized to 2243.2 K.

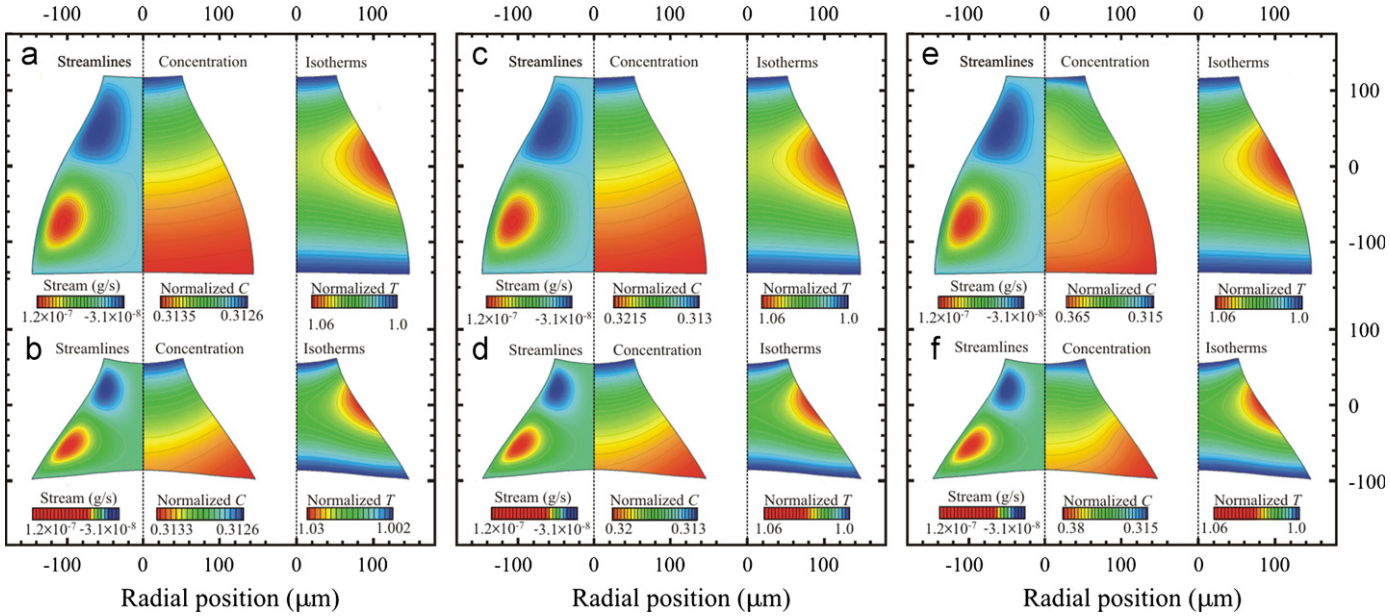

Fig. 4. The streamlines (left), normalized radial concentration of Cr ions (middle), and isotherms (right) in the miniature melt zones at high (top row) and low (bottom row) P_{allow} for $R_{\%}$=35% while K=3.2, $\partial\gamma/\partial T = -3.5\times10^{-2}$ dyn cm^{-1} K^{-1} and D=(a)(b) 10^{-1}, (c)(d) 10^{-2}, and (e)(f) 10^{-3} cm^2 s^{-1}.

smooth and convex outward, respectively. A parabolic-like profile can be obtained when $R_{\%}\neq100\%$. It is viable to adjust the shape of air/melt interface and the distribution of mass or diffusion flow rate as well as $R_{\%}$, especially the shape of growth front, to obtain a desirable radial profile of concentration as well as that of refractive index for light guide devices or active devices.

Fig. 4 shows how diffusion affects the dopant distribution by adjusting the order of magnitude of D for 10^{-1}, 10^{-2}, and 10^{-3} cm^2 s^{-1}. The thermocapillary convection (TC) compared to dopant diffusion velocity cannot be neglected and then results in the reverse radial dopant profile are compared with the experimental one in Fig. 2(a) if D is smaller than the order of 10^{-3} cm^2 s^{-1}. There is no difference when D is higher than the order of 10^{-2} cm^2 s^{-1}, but it is noted that $D=10^{-1}$ cm^2 s^{-1} is too high to be a characteristic of a liquid. Therefore, $D=10^{-2}$ cm^2 s^{-1} is the reasonable order and consistent with the experimental observation. It implies that the diffusion velocity of all Cr ions as much lighter solute is higher than that of mass flow rate (F_m) in the YAG streamlines as much heavier solvent. The weight ratio of these two particles is ~8.75%. The temperature distribution and then the streamline pattern do not influence the dopant distributions.

Fig. 5 shows how convection affects the dopant distribution by changing the order of magnitude of surface-tension–temperature coefficient $\partial\gamma/\partial T$ for 0, -3.5×10^{-4}, and -3.5×10^{-2} dyn cm^{-1} K^{-1}. F_m increases as $\partial\gamma/\partial T$ is increased for TC. Stable double eddies are formed when F_m reaches the order of 10^{-6}–10^{-5} g s^{-1}. For pure YAG, F_m is on the order of 10^{-5}–10^{-4} g s^{-1}. The experimental radial dopant profiles of grown crystal fiber indicate that the buoyancy-driven convection between Cr and YAG, which follows the mass flow of YAG, should be neglected here. The radial dopant profile is steeper at P_{allow}=1.68 W because of the zone shape. The concentration level is shifted at various $\partial\gamma/\partial T$ values because TC influence in the melt cannot be neglected at low P_{allow} or smaller melt zone. The radial profiles

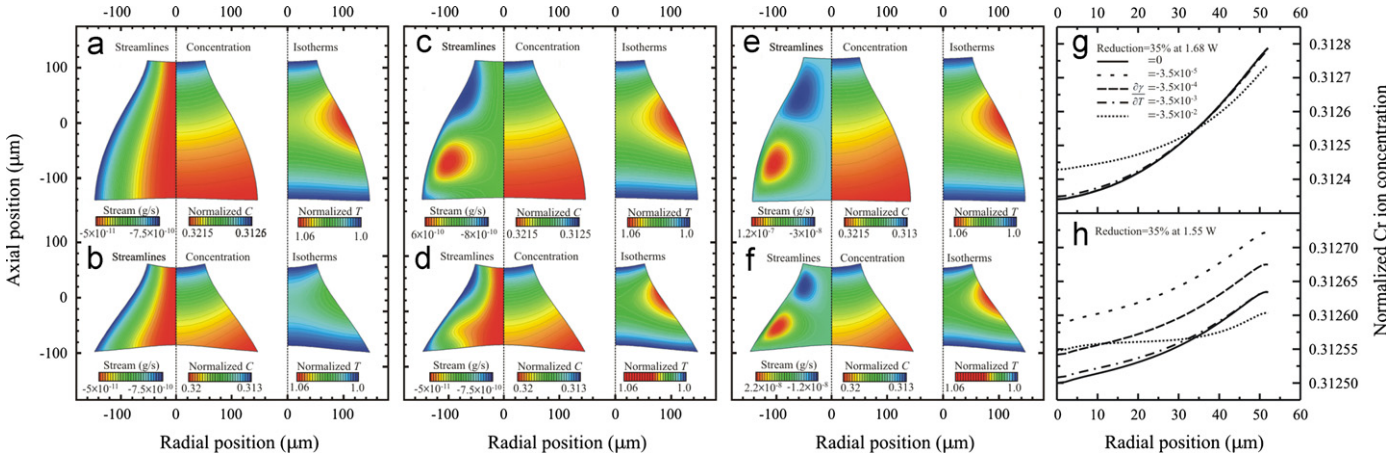

Fig. 5. The streamlines (left), normalized radial concentration of Cr ions (middle), and isotherms (right) in the miniature melt zones at high (top row) and low (bottom row) P_{allow} for $R_{\%}=35\%$ while $K=3.2$, $D=10^{-2}$ cm^2 s^{-1} and $\partial\gamma/\partial T$=(a)(b) 0 , (c)(d) -3.5×10^{-4}, (e)(f) -3.5×10^{-2} dyn cm^{-1} K^{-1}. The corresponding normalized radial dpaont profiles at the growth front are at (g) 1.68 W and (h) 1.55 W.

become smooth in Fig. 5(g)(h) if $\partial\gamma/\partial T$ is higher than -3.5×10^{-3} dyn cm^{-1} K^{-1} since the strong enough TC with clockwise upper eddy to collect the dopant ions from periphery to center near the growth front to form a smooth profile. For doped YAG, $\partial\gamma/\partial T$ is $<-3.5\times10^{-2}$ dyn cm^{-1} K^{-1} exactly.

5. Conclusions

Based on the experimental confirmation of melt shapes and the further analysis of heat transfer and fluid flow, the radial concentration profiles of Cr ions are analyzed for growing high quality Cr:YAG single-crystal fiber devices. The radial dopant profiles at growth front in simulations are consistent with that of grown crystal fibers in *ex-situ* measurements. From the macroscopic view, it is viable to adjust the shape of air/melt interface, the distribution of mass flow rate, and especially the shape of growth front to obtain a desirable radial dopant profile. $D=10^{-2}$ cm^2 s^{-1} is the reasonable order and consistent with the observation, which indicates that the temperature distribution and streamline pattern do not influence the dopant distributions. The level of average dopant concentration might be raised with a low enough magnitude of $\partial\gamma/\partial T$ at low P_{allow}, but a smoother profile is obtained. More precise quantitative comparison for different dopants in YAG, such as Nd:YAG crystal with K is 0.18 [26], can be investigated further by including the real concentration of source rod as the initial value. Crystallization dynamics, such as curvature-induced undercooling effect, also needs to be considered in microscopic view in the future.

Acknowledgment

This work was supported in part by National Science Council, Taiwan, ROC, under the contracts NSC-96-2628-E-002-042-MY3 and NSC-99-2120-M-002-014-MY1.

References

[1] R.S. Feigelson, Mater. Sci. Eng. B 1 (1988) 67.
[2] J.D. Love, W.M. Henry, W.J. Stewart, R.J. Black, S. Lacroix, F. Gonthier, IEE Proc. J. Optoelecton. 138 (1991) 343.
[3] C.N. Tsai, Y.S. Lin, K.Y. Huang, Y.S. Lin, C.C. Lai, S.L. Huang, Jpn. J. Appl. Phys. 47 (2008) 6369.
[4] M.J.F. Digonnet, C.J. Gaeta, H.J. Shaw, J. Lightwave Technol. LT-4 (1986) 454.
[5] C.Y. Lo, P.L. Huang, T.S. Chou, L.M. Lee, T.Y. Chang, S.L. Huang, L. Lin, H.Y. Lin, F.C. Ho, Jpn. J. Appl. Phys. 41 (2002) L1228.
[6] C.C. Lai, K.Y. Huang, H.J. Tsai, K.Y. Hsu, S.K. Liu, C.T. Cheng, K.D. Ji, C.P. Ke, S.R. Lin, S.L. Huang, Optics Letters 34 (2009) 2357.
[7] G.M. Davis, I. Yokohama, S. Sudo, K. Kubodera, IEEE Photonic Technol. Lett. 3 (1991) 459.
[8] C.Y. Lo, K.Y. Huang, J.C. Chen, C.Y. Chuang, C.C. Lai, S.L. Huang, Y.S. Lin, P.S. Yeh, Opt. Lett. 30 (2005) 129.
[9] C.Y. Lo, K.Y. Huang, J.C. Chen, S.Y. Tu, S.L. Huang, Opt. Lett. 29 (2004) 439.
[10] J.C. Chen, Y.S. Lin, C.N. Tsai, K.Y. Huang, C.C. Lai, W.Z. Su, R.C. Shr, F.J. Kao, T.Y. Chang, S.L. Huang, IEEE Photon. Technol. Lett. 19 (2007) 595.
[11] K.Y. Huang, K.Y. Hsu, S.L. Huang, IEEE Lightwave Technol. 26 (2008) 1632.
[12] L.M. Lee, S.C. Pei, D.F. Lin, M.C. Tsai, T.M. Tai, P.C. Chiu, D.H. Sun, A.H. Kung, S.L. Huang, J. Opt. Soc. Am. B 24 (2007) 1909.
[13] D.H. Yoon, Opto-electronics Rev. 12 (2004) 199.
[14] M. Matsukura, Z. Chen, M. Adachi, A. Kawabata, Jpn. J. Appl. Phys. 36 (1997) 5947.
[15] R.S. Feigelson, J. Cryst. Growth 79 (1986) 669.
[16] M. M. Fejer, Ph.D. dissertation thesis (1986) Stanford University, USA.
[17] G.W. Young, J.A. Heminger, J. Cryst. Growth 178 (1997) 410.
[18] C.W. Lan, S. Kou, J. Cryst. Growth 108 (1991) 351.
[19] P.Y. Chen, C.L. Chang, K.Y. Huang, C.W. Lan, W.H. Cheng, S.L. Huang, J. Appl. Crystallogr. 42 (2009) 553.
[20] P.Y. Chen, C.L. Chang, K.Y. Huang, C.W. Lan, W.H. Cheng, S.L. Huang, Jpn. J. Appl. Phys. 48 (2009) 115504.
[21] K.Y. Huang, K.Y. Hsu, D.Y. Jheng, W.J. Zhuo, P.Y. Chen, P.S. Yeh, S.L. Huang, Opt. Express 16 (2008) 12264.
[22] S. Ishibashi, K. Naganuma, I. Yokohama, J. Cryst. Growth 183 (1998) 614.
[23] C.W. Lan, C.Y. Tu, J. Cryst. Growth 223 (2001) 523.
[24] C.W. Lan, S. Kou, J. Cryst. Growth 132 (1993) 578.
[25] J.C. Chen, C.Y. Lo, K.Y. Huang, F.J. kao, S.Y. Tu, S.L. Huang, J. Cryst. Growth 274 (2005) 522.
[26] B. Henderson, Ralph H. Bartram, Crystal-field Engineering of Solid-state Laser Material, Cambridge University Press, 2000 83-85.
[27] V.J. Fratello, C.D. Brandle, J. Cryst. Growth 128 (1993) 1006.